Ceria-stabilized zirconia-based composites printed by stereolithography: Impact of the processing method on the ductile behaviour and its transformation features

Sylvain Fournier, Jérôme Chevalier, Guilhem P. Baeza, Christophe Chaput, Eric Louradour, Philippe Sainsot, Jérôme Cavoret, Helen Reveron

Journal Pre-proof

Ceria-stabilized zirconia-based composites printed by stereolithography: Impact of the processing method on the ductile behaviour and its transformation features

Sylvain Fournier, Jérôme Chevalier, Guilhem P. Baeza, Christophe Chaput, Eric Louradour, Philippe Sainsot, Jérôme Cavoret, Helen Reveron

PII: S0955-2219(22)00869-X
DOI: https://doi.org/10.1016/j.jeurceramsoc.2022.11.006
Reference: JECS 15257

To appear in: *Journal of the European Ceramic Society*

Received date : 31 August 2022
Revised date : 19 October 2022
Accepted date : 2 November 2022

Please cite this article as: S. Fournier, J. Chevalier, G.P. Baeza et al., Ceria-stabilized zirconia-based composites printed by stereolithography: Impact of the processing method on the ductile behaviour and its transformation features, *Journal of the European Ceramic Society* (2022), doi: https://doi.org/10.1016/j.jeurceramsoc.2022.11.006.

Ceria-stabilized zirconia-based composites printed by stereolithography: Impact of the processing method on the ductile behaviour and its transformation features

Sylvain Fournier[a], Jérôme Chevalier[a], Guilhem P. Baeza[a], Christophe Chaput[b], Eric Louradour[b], Philippe Sainsot[c], Jérôme Cavoret[c], Helen Reveron[a]

[a] *Univ Lyon, INSA Lyon, Universite Claude Bernard Lyon 1, CNRS, MATEIS, UMR5510, Villeurbanne, 69621, France*
[b] *3DCERAM Sinto, 4, rue du Parc de Maison Rouge, ZA Maison Rouge, Bonnac-la-Cote, 87270, France*
[c] *Univ Lyon, INSA Lyon, CNRS, LaMCoS, UMR5259, Villeurbanne, 69621, France*

Abstract

A commercial composite powder was used to develop a new paste for stereolithography processing (SLA) of dense 11Ce-TZP-based composites containing 8 vol.% of alumina and 8 vol.% of strontium aluminate. The same powder was used to prepare reference ceramics by conventional Cold Isostatic Pressing (CIP) and sintering. The use of SLA gave rise to a microstructure containing larger strontium aluminate clustering surrounded by zirconia grains devoid of alumina particles, which appeared embedded in a matrix of zirconia-alumina grains. This slightly more heterogeneous microstructure favored the formation of a greater number of thinner transformation bands, causing a larger plastic deformation in SLA samples (failure strain of 0.65 % instead of 0.35 % for CIP samples), without compromising characteristic strength (σ_0 = 560 and 586 MPa respectively) . Thus, SLA does not affect the ductile behaviour that characterizes this type of ceramics and appears as a very promising method for the development of custom-made ceramic prostheses.

Keywords: Stereolithography, Composites, Zirconia, Plasticity, Phase transformation

1. Introduction

Ceria (CeO_2) stabilized zirconia (ZrO_2)-based composites are very promising candidates for the development of patient-specific biomedical implants [1], owing to their biocompatibility, high toughness, certain amount of ductility and excellent resistance to Low-Temperature Degradation [2, 3]. Their ductile behaviour is driven by their well-known stress-induced tetragonal (t) to monoclinic (m) zirconia phase transformation, which is accompanied by a volume expansion of 3-5 % and shear strain reaching 16 % [4]. Hence, after loading this type of ceramics above the critical stress for triggering $t-m$ transformation (${\sigma_c}^{t-m}$), permanent strain is obtained with no loss in stiffness and no associated microcracking [5]. The development of zirconia-based composites that show a significant amount of ductility without damage implies to reach a sufficient propensity to undergo $t-m$ phase transformation at ambient temperature. To optimize or adjust this $t-m$ transformability, the concentration of ceria within the zirconia matrix (Ce-TZP: *Ceria-stabilized Tetragonal Zirconia Polycrystals*) and the quantitiy of secondary added-phases (e.g., Al_2O_3: *Alumina* and $SrAl_{12}O_{19}$: *Strontium-Aluminate*) must be adjusted. The $t-m$ transformability increases with lower fractions of ceria stabilizer and larger zirconia grains [6, 7] resulting in a higher toughness of the material (K_{IC}). However, the relation $\sigma_R - K_{IC}$ passes through a maximum so that it is impossible to increase both properties indefinitely. A compromise must be found according to the required engineering properties [8].

Composites containing 84 vol.% (11 mol.% CeO_2- stabilized zirconia); /8 vol.% (Al_2O_3); /8 vol.% $SrAl_{12}O_{19}$ conventionally processed at industrial scale (by Cold Isostatic Pressing) and sintered in air (1450 $^{\circ}C$ - 1 h), have shown a certain degree of ductility and other interesting features such as the absence of Low Temperature Degradation [2]. Thess composites, often referred as '$ZA_8Sr_8Ce_{11}$' in relation to their composition, are today commercially available under the tradename 'Evocera®'[9]. They present the following grain sizes after sintering: zirconia (Z: 1.0 ± 0.3 μm), aluminate (S: 1.7 ± 0.5 μm length; aspect ratio length/width 5 ± 2) and alumina (A: 0.3 ± 0.1 μm) [2]. When tested in four-point bending (4PB), these composites exhibited a significant strain to failure (i.e., 0.4 %), an onset of non-linearity in the stress-strain curve of 420 MPa (considered as a yield transformation stress or ${\sigma_c}^{t-m}$) and a failure strength of about 600 MPa. The fracture toughness measured by SEVNB was of 10.2 ± 0.2 $MPa\sqrt{m}$ [10].

Upon 4PB loading, the $t-m$ phase transformation occurs through the formation of parallel bands that propagate from the tensile side towards the neutral axis. Their number and size increased with applied stress [11]. The bands exhibited a limited amount of 20-30 vol.% of monoclinic transformed phase (45 vol.% in the band near the rupture), in agreement with previous studies conducted on similar materials. Inside transformed bands, no microcracks were detected by deep microstructural analyses in transformed bands, except for a few microcracked grain boundaries at the samples' surface (< 1 μm depth) [5].

Recent advances in medical imaging and additive manufacturing (AM) technologies have enabled the design and production of complex patient-specific implants and prostheses with optimized design and enhanced functional performances. Selective Laser Sintering (SLS) from biocompatible metals and alloys (e.g., Ti grade 23, Ti-6Al-4V, stainless steel) as well as Ceramic Laser Stereolithography (SLA) from ceramic pastes (e.g., alumina, hydroxyapatite, yttria-stabilized zirconia) have been used for the development of additively manufactured sub-periosteal jaw implants [12], mandibular joint [13] and orbital floor implants [14].

Among the ceramic AM, SLA is one of the commercially available technologies showing the highest dimensional accuracy and tolerances as well as industrial maturity. The process allows the creation of complex 3D objects by consecutive addition of 2D layers of a photopolymerized resin containing ceramic particles. During printing, each layer of typically $20-100$ μm thickness is polymerized by a laser beam, which selectively cures the regions following a STL file (i.e., the translation of the CAD 3D model sliced into a series of 2D layers) until the completion of the 3D piece. Green bodies made of cured polymer and ceramic particles are slowly debinded and then sintered to obtain the final product. However, among the limitations of additive manufacturing of "brittle" ceramic parts, the reduction of their mechanical strength due to delamination issues between adjacent layers [15] and the presence of pores and agglomerates defects [16] that are introduced during printing or the post-processing thermal treatments can be cited. Alternatively, SLA technology appears very promising for the production of "ductile" ceramic composites such as $ZA_8Sr_8Ce_{11}$. Indeed, their excellent intrinsic resistance to defects should be able to guarantee the maintenance of mechanical properties even if certain defects are introduced during AM. Despite the limited litterature on ceria-based ceramics processed by photopolymerization AM techniques [17], there is currently no such photopolymerizable slurry/paste

commercially available.
The present work is conducted with a number of aims in mind. On one hand, we want to develop a SLA paste with $ZA_8Sr_8Ce_{11}$ powder in order to study the feasibility of AM processing of such type of composites, and specifically with a CeraMaker C900 printer (3DCERAM Sinto, France). Another objective of the present work is to compare mechanical behaviour of these composites processed by SLA with that observed in conventionally shaped and sintered materials produced on an industrial scale by a standard powder-mixing route [1]. In other words, we are willing to answer these two questions (1) Is their ductile behaviour compromised or affected by the change of processing and/or post-thermal treatments specific to SLA ?, (2) Can the defect tolerance of Ce-TZP-based composites guarantee the mechanical properties of materials processed through SLA, even if processing defects are still generally of higher quantity and larger size than with conventional fabrication methods ?
In this work, SLA pastes of $ZA_8Sr_8Ce_{11}$ are thus developed using a composite powder. Bars are printed, debinded and sintered to approach microstructural features observed on conventionally processed ceramics. Reference samples are prepared using the same composite powder and isostatic pressing. The mechanical behaviour of these ceramics is studied in four point bending (4PB). The results are discussed based on the tetragonal to monoclinic phase transformation of zirconia governing the ductile behaviour, coupled with extensive optical and scanning electron microscopy analyses.

2. Materials and Methods

2.1. Materials

The studied ceramic composite had a composition of 84 vol.% ZrO_2 (11 mol.%CeO_2), 8 vol.% of Al_2O_3 and 8 vol.% of $SrAl_{12}O_{19}$ (denoted $ZA_8Sr_8Ce_{11}$ hereafter) [5]. A granulated composite powder provided by DOCERAM (Germany) was used as starting material. The Stereolithography (SLA) paste were prepared by dispersing suitable amounts of as-debinded powder (1 *°C/min* - 600 *°C*) with a photoreactive organic mixture (3DCERAM Sinto, France). Preliminary tests showed that it was difficult to polymerize SLA-pastes using the organic formulations developed for yttria-stabilized zirconia-based materials by 3DCERAM Sinto and with a laser wavelength of 355 *nm*. Ce-TZP high absorption at 355 *nm* compared to 3Y-TZP must have a big impact on laser-curing, making it challenging to print parts with

reasonable laser power and time consumption.
ZrO_2 absorbance exhibits a minimal plateau from 340 to > 800 nm, indicating that zirconia is not expected to present absorption issues during printing whether a 355 nm or 405 nm laser is used [18, 19]. Yttria doped zirconia also displays a low absorbance at these wavelengths [20]. The value of CeO_2 absorbance at 405 nm being one third of its value at 355 nm [21] suggests that any SLA-paste prepared from cerium-containing powders will be more easily cured with laser wavelengths well above 340-360 nm. Highly absorbant particles would decrease significantly the overall energy transmitted to the photopolymerizable organic part and the curing depth. Therefore, a higher incident beam wavelength (405 nm) was chosen to avoid the domain of high absorption of Ce-TZP. The polymerizing system (monomers and photoinitiators) were adapted in order to increase paste reactivity at this wavelength.

2.2. Sample preparation

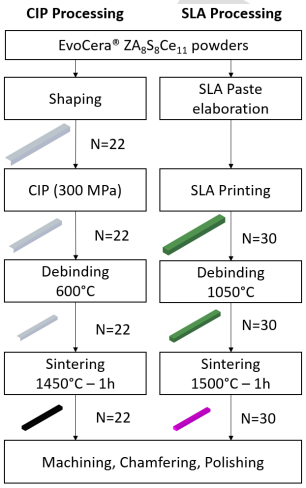

Figure 1: Processing routes followed to prepare CIP and SLA samples

Fig.1 shows schematically the processing routes used for preparing the SLA and reference CIP samples.
SLA specimens were printed using a CeraMaker C900 machine (3DCERAM Sinto, Limoges). Bar-shaped samples (final dimensions $40 \times 4 \times 3$ mm^3) were

printed using a laser wavelength of 405 nm and layer height of 20 μm. At the end of the sterolithography process, samples were cleaned (separated from the uncured paste) using Ceraclean® solvent, (3DCERAM Sinto, France), dried and slowly debinded up to 1050 $^{\circ}C$. This thermal post-treatment allows organic components to degrade at a slow rate, ensuring slow volume shrinkage, limiting residual mechanical stress and other damages on the final sintered samples. Thirty bending specimens (final dimensions $40 \times 4 \times 3$ mm^3) were built horizontally over the building platform (XY plane) so that the fracture plane will be perpendicular to the printed layers.
A SLA debinded bending bar was cut into smaller pieces ($5 \times 4 \times 3$ mm^3) that were sintered at different higher temperatures (1400, 1450, 1500, 1550 and 1600 $^{\circ}C$, at 5 $^{\circ}C/min$ for 1 h) in order to study the sintering behaviour. For each sintering temperature, the geometrical final density was measured, calculated and reported as the percentage of the theoretical density (% t.d.) of Ce-TZP triphasic composites (i.e., 5.861 g/cm^3) and the zirconia grain size was estimated using the linear intercept method and a multiplying corrective factor of 1.56. Additionnaly, a dilatometry experiment (Setaram 92, Switzerland) was also conducted at 5 $^{\circ}C/min$ in air in order to complete the comparison in terms of sintering ability of SLA vs CIP samples and help chosing the optimal sintering temperature.
For comparison, CIP samples (final dimensions $40 \times 4 \times 3$ mm^3) were produced by Cold Isostatic Pressing (CIP at 300 MPa) using the same granulated powder than in SLA (DOCERAM, Germany). Specimens were debinded (600 $^{\circ}C$ for 1 h, 1 $^{\circ}C/min$) and sintered at 1450 $^{\circ}C$ for 1 h (5 $^{\circ}C/min$) in order to develop reference materials showing comparable zirconia grains size (1.0 ± 0.3 μm) and density [11, 5]. A total of 22 bars of this reference material were produced.

2.3. Characterization

Ceramic final microstructures were investigated by means of Scanning Electron Micoscopy (SEM; Zeiss SUPRA VP55, Switzerland and Vega 3 Tescan, Czech Republic) at low voltage on surfaces polished down to 0.03 μm colloidal silica suspension without any thermal etching treatment nor gold coating. For fractography purposes, SEM observations were also conducted on as-fractured surfaces of all tested samples (Vega 3 Tescan, Czech Republic). Microstructural features were measured from SEM high magnification images and analyzed (ImageJ, National Institutes of Health, USA). The zirconia grain size was estimated using the linear intercept method and a multiply-

ing corrective factor of 1.56. The strontium aluminate grains/platelets and clusters (called hereafter SrAl) areas, circularity, and their distance to closest alumina grains (shell width) were measured. X-ray Computed Tomography (XCT) analysis was performed on SLA and CIP samples to identify typical processing defects and characterize their size and relative content (Phoenix V tome xs tomograph; General Electric TM, USA). XCT measurements were carried out using a voxel size of 8 μm^3. The studied volume dimensions were: $716 \times 1240 \times 602$ μm^3 (i.e., 0.534 mm^3). Larger volumes were difficult to study because of the zirconia X-ray high absorption. The scanned volumes were processed using ImageJ, applying a contrast threshold and a minimum diameter filter (7 μm) in order to differentiate noise from small lower density zones and measure their dimensions. Each (x;y) point's darkest value of all z planes was projected on a single plane, revealing all the defects in a single image.

Final densities were precisely evaluated in SLA and CIP bars by Archimedes' method according to the C373-88(2006) ASTM standard.

Four-point bending (4PB) tests were carried out using a universal hydraulic testing machine (INSTRON 8562, Nordwood, USA) equipped with a Linear Variable Differential Transformer (LVDT) for displacement measurements. Monotonic loading tests up to failure were performed using a 35 mm outer span and 10 mm inner span at a cross-head speed of 0.5 mm/min. For transformation bands observation, loading-unloading tests were carried out at a lower cross-head speed of 0.1 mm/min. Prior mechanical tests, all specimens were machined, chamfered and polished down to a 16 μm diamond paste (monotonic tests) following the ISO 6872 standard for dental ceramics [22]. Chamfering has been conducted manually, such as few samples have bigger chamfers than advised by the standard. The strength was calculated for each specimen considering their dimensions. Chamfers were not considered for it as a simple calculation of inertia moment showed the reduced impact (less than 4%) compared to a non-chamfered bar and to a bar with maximal standard chamfers (less than 3%). In selected samples subjected to loading-unloading tests, both tensile and front side surfaces were mirror-polished down to 0.03 μm in order to characterize transformations bands at different levels of stress. All mechanical tests were performed at room temperature ($22 \pm 2°C$) in air. Among 30 SLA samples, 5 were not considered for Weibull analysis because of extended straight cracks probably formed during sintering and 5 were reserved for preliminary, dilatometry and loading-unloading tests. First, Weibull analysis was applied to the strength

data following the ISO Standard 6872. Another approach was tested in order to give the same weight to each point of the distribution for curve fitting. This second method (called hereafter exponential fit) is the fitting of Weibull exponential function $P_f = 1 - exp(-(\frac{\sigma}{\sigma_0})^m)$ by Levenberg Marquardt method with OriginLab software (North Hampton, USA). For both Weibull analysis methods, confidence limits -95 % and +95 % of Weibull modulus (m) and characteristic strengths (σ_0) were estimated from Davies' method [23]. Finally, a *Student t-test* with parameters k(degree of freedom)= 1 and α (risk factor) = $0,05$*h was performed in order to compare SLA and CIP strength distributions. The Young's modulus (E) of different ceramics was estimated by a resonance vibration method (ASTM C1259-01, Grindo-Sonic tester).
Transformation bands were characterized by optical microscopy (Hirox RH-2000, Japan) carried out in dark mode. Tensile and front side surfaces were observed after each loading/unloading cycle until the failure. From the obtained pictures, the number of bands on tensile and front side surfaces as well as their transformation depth on the front side surface were characterized. Additionally, transformation bands evolution was characterized by white-light Vertical Scanning Interferometry (VSI) measurements using a S-Neox (Sensofar, Terrassa, Spain) 3D non-contact optical profiler machine, which combines confocal and interferometry techniques (lateral resolution of 0.26 μm). An objective of 10x with an acquisition area of 1.70×1.42 mm^2 was used with a step of 1.38 μm on the two axes (x and y). Images of the samples were obtained after stitching using an overlapping parameter of 15 %. The acquired data were processed using MountainsMap Universal software (DigitalSurf, Besançon, France). Roughness parameter Ra (arithmetic mean roughness) was given from profiles that are perpendicular to the transformation bands and on the same positions on each scan, in the uniform stress zone between the inner span. On the tensile side, a representative West-East profile was selected in order to get bands height, width and spacing. Sa roughness parameter (arithmetic mean roughness for a surface) was calculated on whole surfaces.
The transformabiliy of zirconia after 4PB tests was studied by XRD analysis performed on as-fractured surfaces of three SLA and one CIP samples. A D8 Advance Bruker AXS diffractometer (Billerica, USA) with Ni-filtered Cu Kα radiation (1.54056 Å) in the 2θ range 27 °- 33 °(step size 0.02 °, step time 2 s) was used. A polished SLA sample surface was also characterized in order to check that the initial tetragonal amount (before the 4PB test), was about 100 %. The 2θ range studied here contains reflections of $(111)_m$,

$(\text{–}111)_m$ and $(101)_t$ peaks used to estimate the volumetric fractions of the $m-ZrO_2(V_m)$ and $t-ZrO_2(V_t)$ phases from the areas (respectively A_m and A_t) of the diffraction peaks as [24]:

$$V_m = \frac{1.311\chi}{1+0.311\chi} \; and \; V_t = 1 - V_m$$

Where,

$$\chi = \frac{A_m(-111) + A_m(111)}{A_m(-111) + A_m(111) + A_t(101)}$$

3. Results and Discussions

3.1. Sintering and microstructural features

The linear shrinkage of debinded-SLA and CIP samples is shown in Fig.2-a. These results demonstrate that in both ceramics the shrinkage starts around 1100 $^{\circ}C$ (same onset of sintering temperature). For the SLA samples, the densification is not complete even at 1600$^{\circ}C$ (i.e., the shrinkage still goes on during the first 25 min of the dwell step), whereas for CIP, the sample is fully dense from 1450 $^{\circ}C$. The estimated densities plotted versus the temperature in Fig.2-b reveal that at 1350 $^{\circ}C$, CIP ceramics were 97 % dense while SLA-ceramics were only 87 %. The comparison indicates obviously that high-densities can be achieved for CIP composites at lower sintering temperatures than SLA. Therefore, it was chosen to sinter the SLA samples at 1500 $^{\circ}C$ for $1h$, while keeping 1450 $^{\circ}C$ for $1h$ for CIP ones to use the same conditions as in our previous works [5, 11]. Sintering CIP samples at temperatures lower than 1450 $^{\circ}C$ would have modified the propensity to $t-m$ phase transformation and thus the mechanical behaviour. From these results, it is clear that SLA process has an effect on the sinterability of the composite powder. The onset temperature of sintering is probably not impacted because SLA and CIP ceramics were processed using the same composite powder as raw material. However, at higher temperatures, the observed differences could arise from a different organization of the ceramic particles and the porosity size/distribution due to the applied shaping method and the removal of an important amount of organics during the debinding step. In spite of these differences in shrinkage, SLA ceramics sintered at 1500 $^{\circ}C$ - 1 h showed satisfying densification and zirconia grains size of 0.77 ± 0.14 μm remaining close to CIP's (0.82 ± 0.12 μm) (Table 1 and Fig.2). The bending bars processed by SLA and debinded were thus sintered at 1500 $^{\circ}C$ for 1 h.

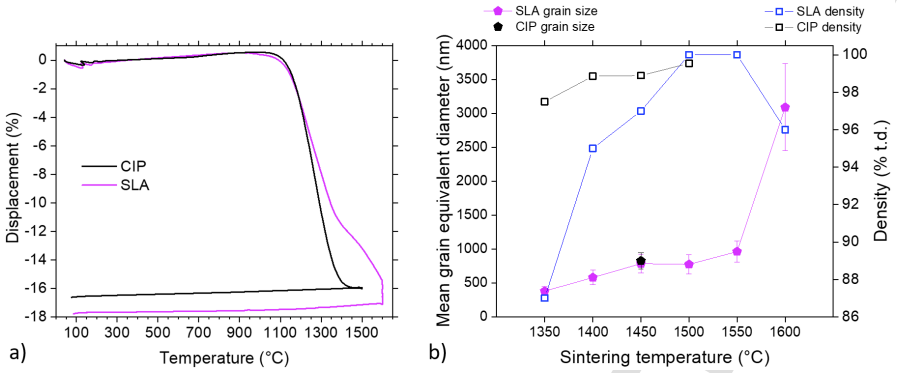

Figure 2: a) Comparison of CIP and SLA dilatometry shrinkage evolution during sintering b) Grains size and geometrical density evolution with sintering temperature; for comparison CIP density values measured by Archimedes method were included to this figure [25]

Almost no monoclinic phase was detected in all sintered ceramics indicating that the tetragonal phase could be maintained after sintering of zirconia.

Table 1: Processing characteristics, final density and mean zirconia grain sizes for SLA and CIP bending bars

Samples	Processing	Debinding (air)	Sintering (5°C/min, air)	Archimedes' final density (% t.d.)	Mean zirconia grain size (μm) (± SD)
SLA 1500°C	SLA	1050°C (slow)	1500°C - 1h	98.8	0.77±0.14
CIP 1450°C	CIP (300 MPa)	600°C - 1h (1°C/min)	1450°C - 1h	98.9	0.82±0.12

One should note that the sintering cycle chosen on the basis of preliminary tests leads to SLA ceramics with almost the same characteristics of density, full-stabilization and zirconia grain size. In order to study differences between SLA and CIP processed ceramics microstructures, some representative samples were submitted to SEM characterization. In Fig.3, the SEM micrographs carried out on polished tensile surfaces show highly dense microstructures exhibiting the zirconia grains of the matrix (light gray), the alumina (round-shaped black grains) and the strontium aluminate (plate-like black grains) secondary phases.

These SEM observations clearly indicate that microstructural features of composites are slightly but significantly different after the two different processing routes, in particular regarding the strontium aluminate grains (SrAl) that appear forming more aggregated clusters in SLA samples than in CIP (Fig.3). Differences observed in Fig.3 were confirmed by images analyses performed with ImageJ, as displayed in Table 2. SLA samples show larger SrAl clusters than CIP while keeping a similar aspect ratio, resulting in a more heterogeneous microstructure in SLA samples than in CIP but with similar fine zirconia grains.

Table 2: SEM strontium aluminates measured characteristics from SEM images analyses table

Sample	SrAl area mean [min;max] (μm^2)	Circularity*	Shell width** between SrAl and alumina particles (μm)
SLA	11.3 [0.4 ; 82.2]	0.23	2.0
CIP	3.7 [1.3 ; 12.1]	0.28	1.6

**A circularity value of 1.0 indicates a perfect circle and as the value approaches 0.0, it indicates an increasingly elongated polygon.*

*** The shell width is the area between SrAl platelets and the closest alumina grains. It corresponds to a zone exclusively composed of zirconia grains.*

These microstructural differences may have been caused by the thermal treatments applied to the SLA processed bending bars in order to reach high density (i.e., a slow debinding up to 1050 $^{\circ}C$, followed by a sintering at higher temperature than CIP) and/or to the SLA processing itself.
We have also observed that the clustering of strontium aluminates leads to an increase of the surrounding zirconia grains size and the disappearance of alumina particles in these regions (shell width) (Fig.3, Table 2). The shape of some SrAl clusters on this figure suggests that alumina grains diffused from surrounding zones towards the cluster. All these elements suggest that alumina grains are likely absorbed by SrAl during sintering, creating larger SrAl structures. Moreover, the shell width around SrAl and SrAl clusters area are larger in SLA samples (Table 2). This alumina migration phenomenon seems to be stronger in SLA processed ceramics.

Palmero et al.[2] studied microstructural development of similar composite compositions (i.e., Ce-TZP, alumina and strontium aluminates) prepared from commercial zirconia powders coated with inorganic precursors of secondary phases, treated thermically and sintered. They found that optimized

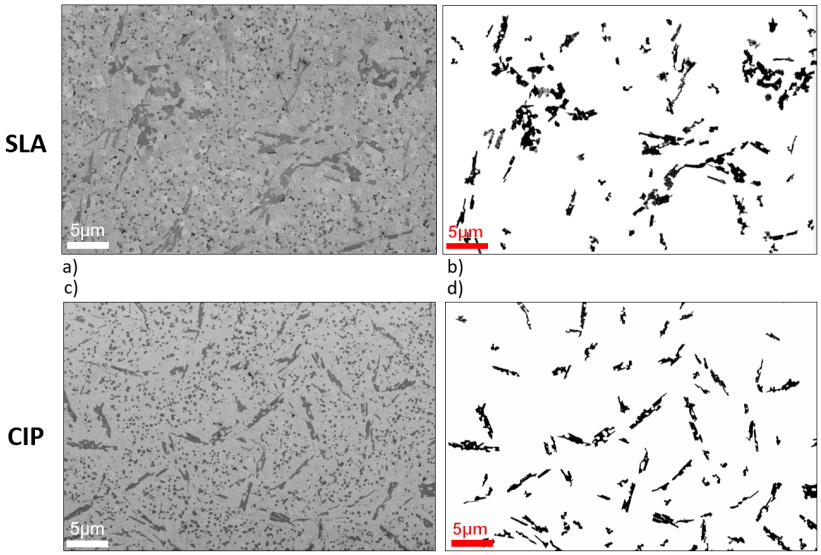

Figure 3: a) SEM micrography of a SLA - 1500 $^{\circ}C$ - 1 h sample surface b) Filtered image with biggest elongated entities containing SrAl c) SEM micrography of a CIP - 1450 $^{\circ}C$ - 1 h sample surface d) Filtered image with biggest elongated entities containing SrAl

pre-thermal treatment of the powder allowed the crystallization of secondary phases and the development of the hexagonal strontium aluminate $SrAl_{12}O_{19}$ during sintering. The strontium hexa-aluminates were characterized by a mean length of 0.4 ± 0.3 μm, significantly lower than what can be obtained from commercial powders processed by CIP or SLA [2]. Preliminary SLA samples sintered at 1500 $^{\circ}C$ - 1 h SEM characterization (not shown here) showed the occurrence of hexagonal-type crystals, that could be related to the formation of $SrAl_{12}O_{19}$. However, other aluminate phases are stable in the system $SrO - Al_2O_3$ such as $SrAl_2O_4$, $Sr_3Al_{12}O_6$ and $SrAl_4O_7$ for which their doping with cerium has also been reported [26, 27]. Owing to the complexity of the elongated phase observed in Fig.3-b;d, which seems to drag/dissolve alumina particles, an in-depth study by TEM would be necessary in order to identify the exact nature and composition of larger aluminates obtained in the present work.

Besides, high-magnification SEM analyses performed on polished samples

showed that independently of the shaping method (SLA or CIP), dense ceramics with no major processing flaws were obtained. In order to identify if some printing or processing defects were created at a higher scale, XCT and low-magnification SEM on fractured surfaces were carried out (Fig.4). Tomography analysis revealed that SLA process led to a ceramic containing a larger amount of XCT-detected low-density zones than CIP samples. However, these defects represent less than 0.1 % of the analyzed volume (Fig.4-c) and these defects do not appear to have a particular orientation. In SLA and CIP ceramics, a similar mean sphericity seems to indicate that, such elongated defects would not be linked to SLA technology itself. It is to note that the filtered XCT scans only reveal defects larger than 7 μm diameter, which may explain the difference with Archimedes porosity content.
In CIP ceramics, only one defect was clearly observed in the analyzed volume and the maximum equivalent defect diameter was about 30 μm. In comparison, higher amount of defects (mainly low-density zones) were detected in SLA sample with a maximum spherical equivalent diameter closer to 50 μm. The Fig.4-e shows a typical zone of lower density that can be found in SLA ceramics.
At lower magnification, some straight cracks were observed on fractured surfaces of SLA 4PB tested ceramics (Fig.4-d). These straight cracks always originated from the side wall of the bending bars and were present in the samples before submitting them to mechanical tests (so after sintering and machining steps). It is well known that debinding is one of the most critical step in SLA and often the source of cracks [28, 29]. The post-processing heat treatments must still be optimized to avoid the formation of this type of defects in the final Ce-stabilized composite ceramics. Moreover, in the SLA fractured surfaces, it was impossible to distinguish the printed layers, and therefore, no classical delamination defects were found.

3.2. Study of stress-strain behaviour

Typical stress-strain curves obtained from 4PB tests for the CIP reference (black curve) and for SLA ceramics (colored ones) are shown in Fig.5-a. Both SLA and CIP samples show a similar elasto-plastic behaviour. The ultimate strength of most of SLA samples was comprised between 500 and 600 MPa and, compared to CIP, higher strain to failure was even achieved (i.e., until 0.65 instead of 0.35 %). Regarding the slope of the SLA stress-strain curves, after reaching the plateau associated to the elastic region, it starts to decrease at $\approx$ 310 MPa (Fig.5-a) against $\approx$ 350 MPa for the CIP

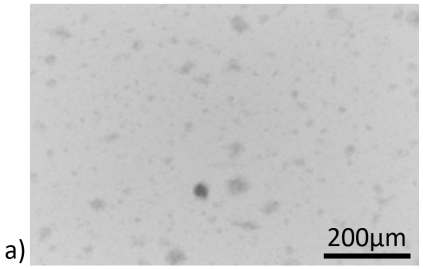

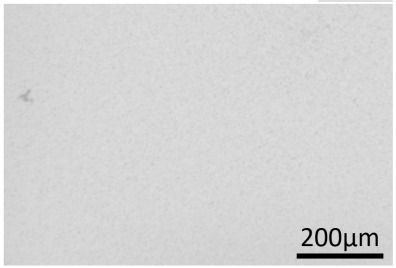

c)

Sample	Grey zones volumic percentage	Sphericity	Equivalent diameter of biggest grey zone (μm)
SLA	0.095 %	0.77	47.4
CIP	0.009 %	0.75	30.7

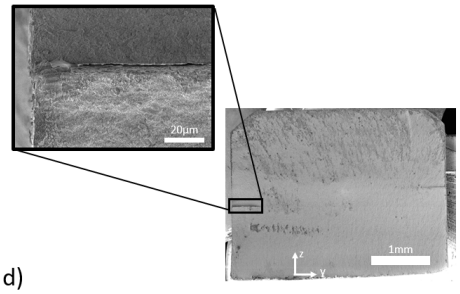

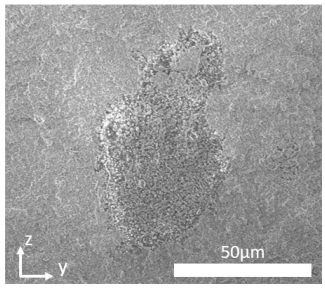

Figure 4: Tomography stacked views (all defects displayed on a plane) of ceramic samples a) SLA printed b) CIP processed c) XCT quantitative analysis d) SEM of SLA fractured bending bar showing 2 straight cracks that propagate from the side wall towards the volume, parallel to the tensile axis e) SEM of SLA fractured surface showing a lower density zone

sample, in agreement with previous works where the critical transformation stress ${\sigma_c}^{t-m}$ was observed in the 350-420 MPa range [11, 5]. The lower critical transformation stress can be related to a higher transformability of certain zirconia grains, that could be related to the development of a more heterogeneous microstructure in SLA samples.

The load-unload stress-strain behaviour of a SLA ceramic (Fig.5-b) shows that during the plastic deformation, the slope of the curve in the elastic region (i.e., the stiffness) remains unchanged. It confirms that the observed

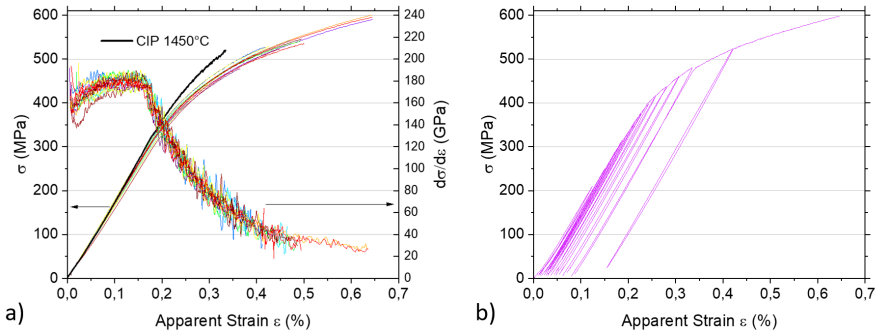

Figure 5: a) Stress-strain curves of SLA printed ceramics obtained in 4-Point Bending. Corresponding apparent slope evolution of SLA curves are also displayed (right y axis). For comparison, the behaviour of a CIP composite ceramic is added. The displayed data concerns N=20 samples tested monotonically at 0,5 mm/min with 35 mm outer span and 10 mm inner span. b) Stress-strain curve of a SLA sample, subjected to an load-unload test increasing

permanent deformation cannot be linked to a possible damaging of the ceramic but rather to the transformation-induced plasticity. In both SLA and CIP materials, ductility is associated to the $t-m$ zirconia phase transformation as described previously [1, 5]. As will be discussed in section 3.4, the first zirconia $t-m$ transformation bands appeared with the loss of linearity, indicating that the critical transformation stress to induce the $t-m$ phase transformation (${\sigma_c}^{t-m}$) is reached in both SLA and CIP ceramics. By considering such differences in ${\sigma_c}^{t-m}$ and strains to failure, one would obtain SLA processed $ZA_8Sr_8Ce_{11}$ composites that are a little more transformable and therefore more deformable than when processed by CIP.
The Young's moduli (E) of ceramics measured by resonance vibration method are summarized in Table 3.

Table 3: Young's modulus of 4PB bars calculated by resonance vibration method

Samples	Processing	E (GPa) (± SD)	Archimedes' final density (% t.d.)
SLA 1500°C	SLA	197±5	98.8
CIP 1450°C	CIP (300 MPa)	218±1	98.9

SLA ceramics showed similar but lower values when compared to CIP ceramics (i.e., $\approx 200\ GPa$ compared to $\approx$ 220GPa). For a given composition, here $ZA_8Sr_8Ce_{11}$ composites, this behaviour would be an indication of a higher degree of porosity, since E is strongly affected by this parameter [30]. However, the observed difference does not seem to be related to the amount of porosity as SLA - 1500 $^{\circ}C$ and CIP - 1450 $^{\circ}C$ showed the same densification degree by Archimedes' method (and a very low amount of porosity observed by XCT in both cases). The decrease in Young's modulus could nevertheless be explained by the formation of more heterogeneous microstructure or the presence of straight cracks discused above in SLA samples. Additional analyses are needed to verify these hypotheses.

3.3. Weibull analysis and Fractography

After 4PB tests, data were analyzed with the Weibull distribution [22, 31] and all SLA tested specimens were subjected to fractography analysis in order to identify, if possible, the origin and the location of the fracture.

Fig.6-a displays Weibull statistical analysis of the strength data obtained in SLA and CIP samples, tested in 4PB configuration.
We applied Weibull analysis to the data set excluding 5 samples that failed at very low stresses ($\sigma_R < 400\ MPa$) because of large pre-existing straight cracks. 5 others samples were reserved for preliminary 4PB tests, dilatometry and loading-unloading 4PB tests, resulting in the analysis of 20 SLA samples results. The Weibull modulus, characteristic strengths, 95 % confidence intervals of the Weibull parameters and the mean strength are summarized in Fig.6-c.

The Weibull modulus (m) is a constant related to the strength distribution. The larger the value of m, the lower the strength variability. Weibull modulus value of brittle yttria-stabilized zirconia ceramics (3Y-TZP) processed by CIP and conventional sintering is generally below 10 [32]. As expected, more transformable and ductile $ZA_8Sr_8Ce_{11}$ composites showed higher values of m. The Weibull modulus of SLA specimens is 16 and that of CIP is 29, whereas the characteristic strength values are 558 and 587 MPa, respectively. Comparatively, the Weibull modulus of SLA processed composites is lower than that of the reference ceramics. However, as the number of tested samples (N= 20 or 22) is too small, it is impossible to really distinguish SLA and CIP Weibull statistics results within a $\pm$ 95 % confidence interval (CI). Moreover, a statistical *Student* test states that the two populations of strength can be declared different if a $\alpha = 5$ % risk is chosen. These two

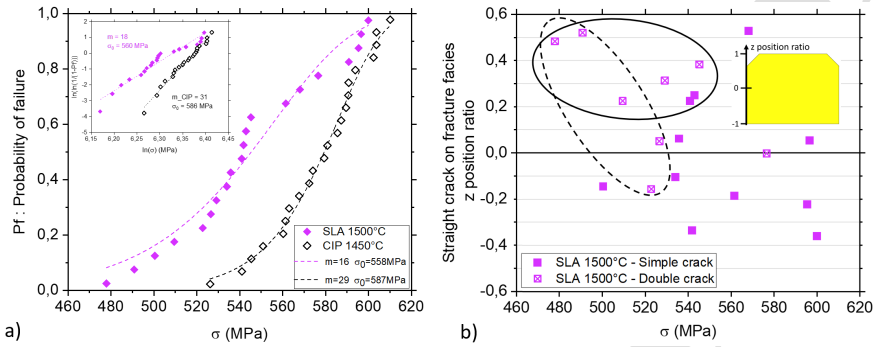

c)

Samples	N: Number of samples	m [95 % CI]	σ_0 [95 % CI] (MPa)
SLA 1500°C	20	16 [10;24]	558 [504;610]
CIP 1450°C	22	29 [18;43]	587 [531;642]

Figure 6: a) Weibull probability of failure of the 4PB strength for SLA printed samples (N=20) and CIP manufactured samples (N=22). Graph inclusion of standard linear regression fitting method. b) For SLA tested samples: effect of the positioning of straight cracks relative to the 4PB neutral axis (z=0) over the strength (stress value at z=1 chamfered surface under tension). Straight cracks positioning was characterized by low-magnification SEM carried-out on as-fractured surfaces. c)Weibull statistic results (obtained by exponential fit) with -95 % to +95 % confidence interval for m (Weibull modulus) and σ_0 (characteristic strength corresponding to the strength at the 63.2 % of Pf).

comparisons suggest that our results are close. A statistical analysis could be conducted later on more samples but for an optimized SLA paste and process.

The fractography analysis performed on SLA samples reveals that 28 out of 30 4PB tested bars exhibit 1 or 2 straight cracks like the ones shown in Fig.4-d. Fig.6-b shows that the higher strength variability observed in SLA samples ($\approx$ 480 to 600 MPa) compared to that in CIP samples ($\approx$ 530 to 610 MPa) can be related to the positioning of this type of defect. The evaluation of the maximal defect size (diameter) that can undergo plastic behaviour from the toughness of $ZA_8Sr_8Ce_{11}$ ceramics (i.e., $10.2MPa\sqrt{m}$ [2, 3]) and the critical transformation stress ${\sigma_c}^{t-m}$ measured for SLA and CIP samples (i.e., $\approx$ 310 and from 350 to 420 MPa, respectively), gives values of around 340 μm for SLA and 200 to 270 μm for CIP (using the theoretical minimal plastic zone at maximal transformation strength $dy = \frac{(K_{IC})^2}{\pi({\sigma_c}^{t-m})^2}$ equation

[33, 34]). It means that observed remanent porosity (Fig.4-c) and lower density zones (Fig.4-e) will not be critical in such very high flaw tolerant materials. Consequently, the observed straight cracks (up to 1 mm deep) appear to be critical regarding failure. Nevertheless, the parallel orientation of these straight cracks with the tensile axis is not favorable to crack opening in the used 4PB test method, making them less prone to cause early failure. When they are more distant to the tensile surface (low values of z), they have less influence on the ultimate strength (points in the continuous circle on Fig.6-b). Double cracks tend to have a larger detrimential effect on strength than single ones (points in the dashed circle on Fig.6-b). Fig.6-a suggests that the higher strength variability observed in SLA samples ($\approx$ 480 to 600 MPa) compared to that in CIP samples ($\approx$ 530 to 610 MPa) can be related to the presence of long cracks. However, thanks to the high ductility of $ZA_8Sr_8Ce_{11}$, the ultimate strength is only slightly reduced on SLA processing samples tested this way. Further optimization of the process and likely debinding should be performed to avoid such long straight craks in SLA samples. Crack inhibition is expected to bring the Weibull characteristics of SLA samples closer to those observed in CIP samples.

Table 4 shows the results of XRD analysis performed on fractured surfaces. Independently of the value of the strength or the processing method, the monoclinic volume fraction transformed was similar and reached 81 to 83 vol.% on the fractured surfaces. The processing by SLA of $ZA_8Sr_8Ce_{11}$ ceramics has no detrimential effect on the transformability of zirconia.

Table 4: XRD monoclinic volumic fraction on 4PB fractured surfaces for SLA and CIP samples. The value obtained on as-sintered ceramic is also reported.

Samples processing	Ultimate strength in 4PB: σ (MPa)	Monoclinic percentage on fractured surface (vol.%)	Monoclinic percentage on as-sintered surface (vol.%)
SLA 1500°C	478	81.7	-
	590	82.3	-
	659	82.6	0
CIP 1450°C	590	81.1	0

3.4. Characteristics of the transformation bands in Four point bending

Fig.7 displays optical micrographs of tensile surfaces obtained during loading-unloading tests performed in a SLA - 1500 $^{\circ}C$ sample until a maximum tensile stress of 427 MPa and after the failure. For comparison, optical images of transformation bands observed in 4PB bars of CIP - 1450 $^{\circ}C$ ceramics are also displayed at 450 MPa and after the failure [11].

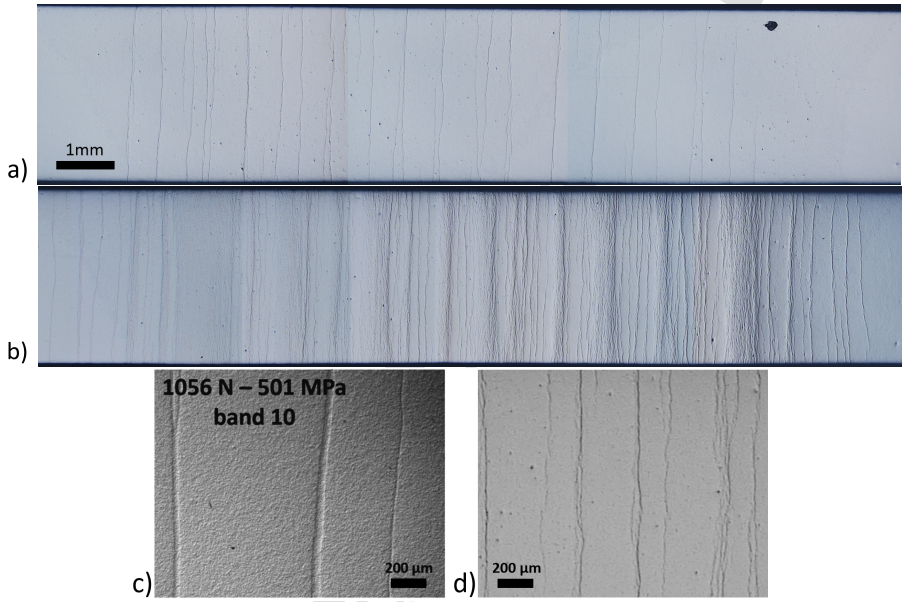

Figure 7: Optical microscopy characterization of the same SLA sample at 2 different stresses (a: 427 MPa, b: 660 MPa). Comparison of the transformation bands features for CIP (c:[11]) and SLA (d) for the same applied stress (c: 501 MPa, d: 503 MPa)

For both types of ceramic samples (SLA and CIP), the first transformation bands appear with the onset of non-linearity observed during loading/unloading cycles. The bands start to form on the tensile side of the samples and then develop towards the neutral axis. At the beginning of the transformation, the first bands are very thin in SLA and CIP ceramics. Nevertheless, the spacing and number of transformation bands as a function of the stress clearly indicate a marked difference in the mechanism of bands formation occurring in SLA samples (Fig.8). In the ceramics processed by CIP,

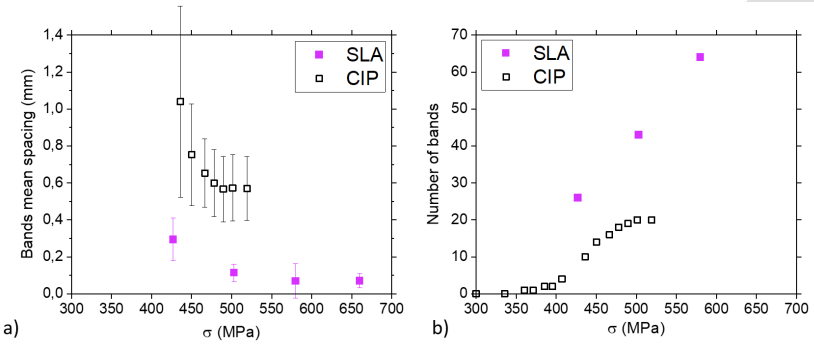

Figure 8: a) Bands mean spacing evolution with incremental loading for SLA samples and CIP samples from Liens et al. works [11]. Bars represent standard deviation of the whole set of values. b) Number of bands evolution on tensile surface for incremental loading compared with CIP data [11]

the width of formed bands increased with increasing the load and the spacing between them becomes more regular and constant close to the load to failure. This saturation of the number of bands before failure (σ >500 MPa) leads to ≈20 bands [11]. The observed progressive transformation-induced plasticity was related to the visible transformation bands that appeared and then increased in width, depth and height with increasing the applied stresses, indicating a nucleation-growth process. On the contrary, for SLA processed samples, the number of newly formed thin bands increased continuously with load. Close to the load to failure, a larger area of the tensile surface was covered with a lot of thinner bands (see Fig.7-b). Therefore, as shown in Fig.8-a, the SLA band spacing decreases with stress and reaches a lower value than in CIP.

Fig.9 displays interferometer 2D topographic profiles at different stresses (tensile side) and 3D views of a band (front side). Even at the beginning of the transformation of SLA samples, some transformed zones are composed of double or triple bands (Fig.9-b). The last two topography images (i.e., at 580 MPa and 660 MPa: Fig.9-b) reveal that close to the load of failure, new bands appear mostly in already transformed zones. On the front side, at low stress levels (σ = 427 MPa), bands are not visible because of the presence of the chamfer Fig.9-c. From 503 MPa, the bands are visible and their number increases with the level of stress. Fig.9-d;e;f show that larger

transformations bands are composed of multiple individual thinner bands and that at 660 MPa, the transformed zones are wider but also exhibit increased volume both on the tensile side and the front side (bands uplift). These topographical changes are linked to the apparition of new thin bands on areas that have already been transformed. The positioning of the bands on the tensile surface corresponds to that of the bands observed on the front side surface. It corroborates that the nucleation of the transformation bands does indeed begin at the tensile surface and then propagates towards the neutral axis.

During load increase, the total area under peaks observed on 2D topographic profiles due to the presence of the transformation bands increased exponentially (Fig.10-a). It suggests that the volume of transformed monoclinic phase in the material also follows this evolution. Moreover, the evolution of the tensile surface roughness (Ra and Sa values) with stress increase show similar results (Fig.10-b). The fact that the surface roughness follows a similar trend corroborates the acceleration of $t - m$ phase transformation at high stress values.

Fig.11 indicates how bands dimensions on the tensile surface (height and width) evolve with stress. It is important to notice that estimated band heights and widths strongly depend on the characterization method. The topography obtained using interferometer devices gives larger values than optical micrographs because the former also take into account the deformed areas around the bands (due to uncompleted transformation or geometrical effect of being close to the band). This is one of the reasons why it is difficult to compare certain band measurements obtained by Liens et al.[11] with the values estimated in this article. Fig.11-a;b show that the increase of the height and width of transformation bands follow the same tendency all along the stress increase. The minimum values of height and width observed in transformed zones (single thinner bands) are indicated by the green line. The boxplot diagrams show that such small bands are also present at high stress values as observed by optical microscopy (Fig.7). Mean and median values of the width and height of the bands are similar at 427, 509 and 580 MPa, meaning that most of the transformed zones are in fact thin bands. This is in good agreement with the increase of the number of bands and the decrease in the spacing between the bands in the [427-580 MPa] stress range previously discussed (see Fig.9). However, the maximum values of height and width showed on the boxplots are higher with increasing stress. It means that some of the transformed zones are growing by addition of new thin bands

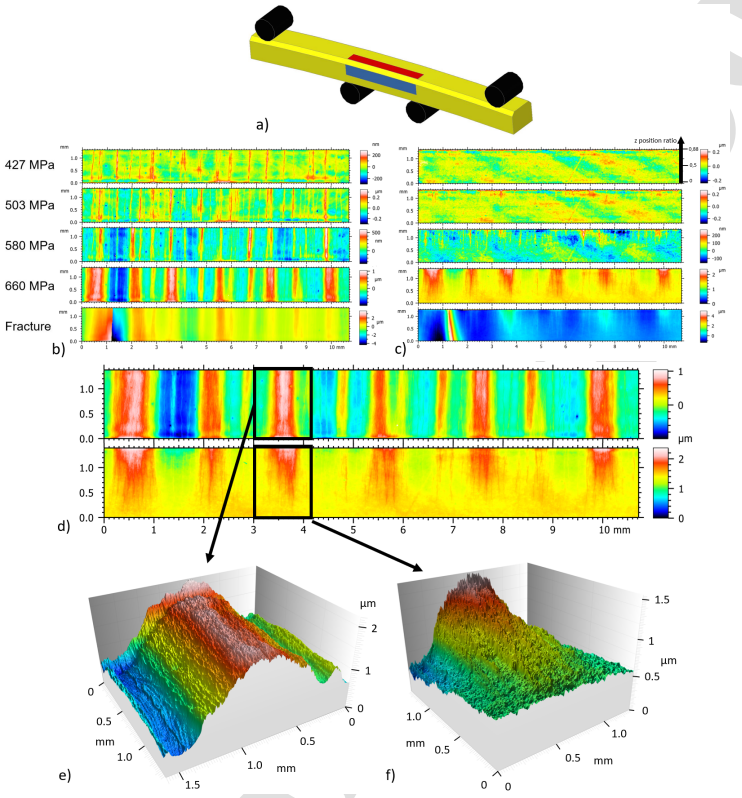

Figure 9: Scheme of a sample subjected to a 4PB test showing interferometer studied surfaces in red (tensile surface) and blue (front side surface). Interferometer topography analysis performed on a SLA - 1500 $°C$ sample tested in 4PB until several incremented maximal stresses on b) tensile surface c) front side surface and d) Interferometer topography images for tensile surface and front side surface at 660 MPa and corresponding 3D views of a transformation zone. Each interferometer graph shows its own relative color scale.

on these already transformed zones. It becomes the principal transformation bands growing mechanism at stresses > 580 MPa where single bands are no longer appearing alone and transformed zones become wider.

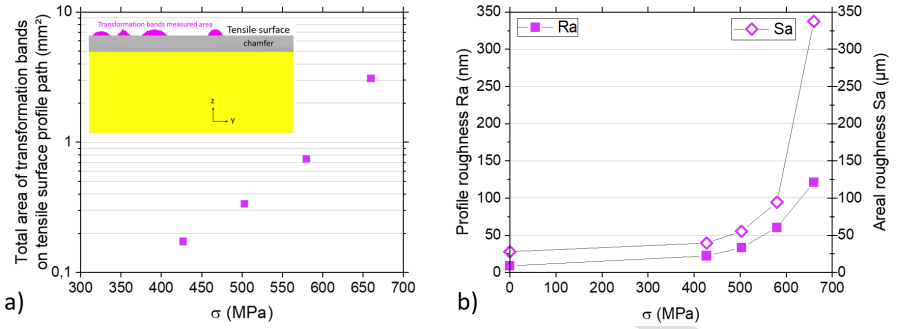

Figure 10: Interferometry analyses on a SLA - 1500 $^{\circ}C$ sample tested in 4PB: a) Total area of transformation bands observed on tensile surface profile path estimated with profile extraction of interferometer mapping b) Roughness evolution (Ra and Sa) of the tensile surface with increasing stress

3.5. Phenomenology of the $t-m$ phase transformation

In CIP samples, once several bands appear, autocatalytic transformation start from these bands, enhancing their dimensions. A stress-shielding zone around the transformation bands impedes the apparition of new bands [11]. Thus, bands grow far from other bands where the applied stress reaches a threshold value (${\sigma_c}^{t-m}$) of about 350 to 420 MPa. Stress relaxation comes from the volume increase of the transformed band due to the $t-m$ transformation and can explain the regular spacing of the bands observed in CIP samples.

In SLA samples, the $t-m$ transformation is quite different since a higher number of thinner bands appear from the beginning of the transformation and continue to be formed at higher stresses. Accordingly, near to the failure point, these thinner bands appear very close to each other, forming wider transformed zones. Therefore, stress-induced transformation bands formation seems to be affected by the presence of preferential nucleation sites or defects indicating an inhomogeneous ${\sigma_c}^{t-m}$. This preferential apparition mechanism is dominant in our SLA samples and no significant autocatalytic growth from existing bands has been observed.

One can understand that several inhomogeneities (zirconia grain size, chemical composition, grain orientation, porosities...) make the transformability (i.e., ${\sigma_c}^{t-m}$) inhomogeneous. Liens et al.[11] proved indeed that small Vick-

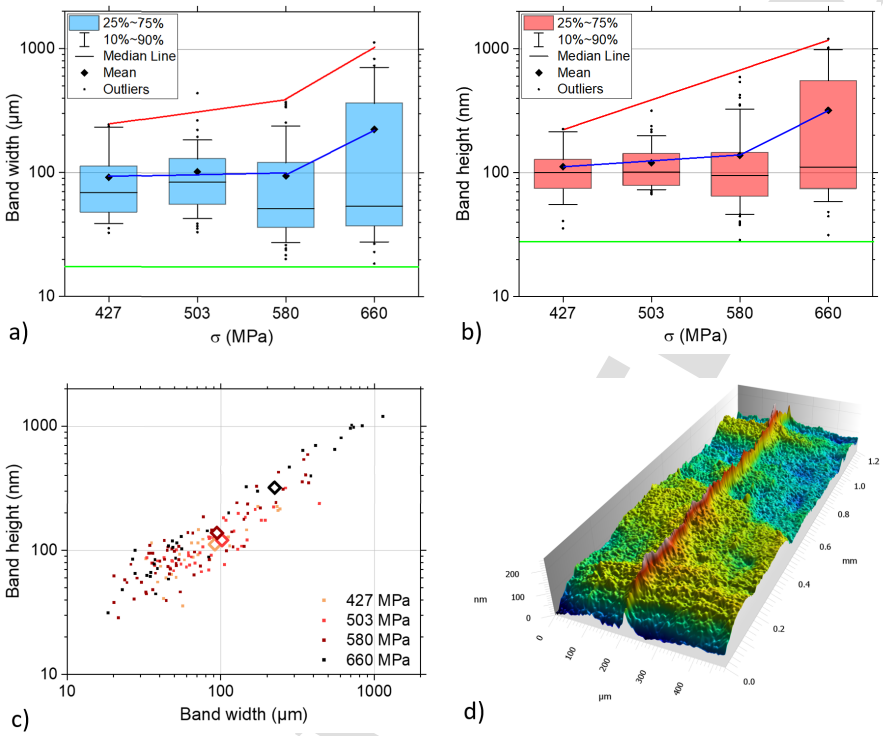

Figure 11: Box plot diagrams of a) band width and b) band height from mapping of an incrementally loaded SLA - 1500 $^{\circ}C$ sample. c) Dispersion of band dimensions and mean values for incremental loading d) Single band of tensile surface of SLA sample topography

ers indents performed on the tensile surface could be catalytic sites for band growth as long as they were spaced enough. Assuming all our tensile surface (between support rollers of the bend fixture) is subjected to the same stress, the transformation will still not be homogeneous. The mechanisms of transformation (autocatalytic, stress release,...) continue to explain the way transformation occurs, through bands apparition (and not an homogeneous percentage of transformed grains all over the surface).
Considering that at the early stage of the transformation, bands grow at different places all over the 4PB tensile surface, microstructural inhomogeneities such as porosities, zones showing lower densification, larger zirconia grains surrounding the aluminate grains or residual stresses could be a source of

preferential sites for bands nucleation. For example, Fig.12 shows that on tested SLA tensile surfaces, transformation bands follow the regions rich in larger SrAl clusters and propagate preferentially inside the surrounding Ce-TZP larger grains devoid of intergranular alumina particles.

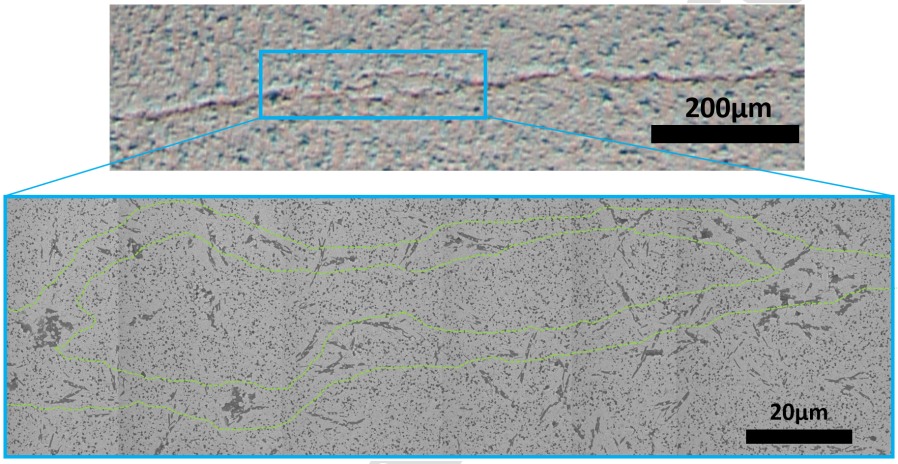

Figure 12: Microstructural features of transformed zones. Bifurcation of a band observed by optical microscope and SEM BSE

The ceramics obtained by SLA therefore show a multitude of fine and more turtous bands which can be linked to the development of a more heterogeneous microstructure. This phenomenon has very interesting implications on the deformation capacity of this type of ceramics (i.e., higher degree of plasticity is reached). It would therefore deserve to be studied more in depth in order to better understand the mechanisms at the origin of this behaviour.

4. Conclusion

In this study, a new Ce-TZP based composite paste was developed in order to prepare dense $ZA_8Sr_8Ce_{11}$ ceramics by stereolithography, using a 405 nm laser. Further developments are necessary to improve the paste formulation, printing parameters and post-processing thermal treatments in order to remove the few straight cracks observed in SLA samples. Yet, SLA composite ceramics exhibited similar density (≈ 99 %) and zirconia grain size (≈ 0.8

μm) as conventional CIP processed ceramics even if SLA as-printed body contained near 50 vol.% of organic media to remove. Thermal characterization showed that SLA samples had to be sintered at higher temperatures and resulted in a more heterogeneous microstructure containing bigger strontium aluminates clusters surrounded by larger zirconia grains and devoid of alumina particles. This phenomenon created zones richer in pure Ce-TZP grains that appear to be preferential sites for the formation of the transformation bands and would be partly responsible for the differences observed in the shape and number of bands. Thus, the greater number of thin bands formed throughout the bending test and covering a greater area of the tensile surface would increase the degree of plastic deformation in the SLA specimens. The answer of question (1) adressed in the introduction is that the transformation-induced plasticity before failure was not compromised by the use of SLA and these samples could even present a greater strain to failure (0.65 % instead of 0.35 % reached in CIP processed ceramics).
The overall mechanical behaviour in bending of SLA ceramics was very similar to that observed in benchmark CIP ceramics, resulting in ceramics combining relatively high characteristic strength (σ_0= 560 and 586 MPa, respectively) and reliability (m=18 and 31, respectively). The answer of question (2) is that even if further optimizations at different steps of the process are still needed, Ce-TZP-based composites processed by SLA showed satisfying mechanical properties. These results show interesting prospects for Ce-TZP based composites additive manufacturing (here by SLA), which has great potential in the development of a new generation of patient-specific maxillofacial, facial and cranial ceramic prostheses.

5. Acknowledgements

Special thanks to CLyM platform (Lyon, France) for the use of their SEM. This work has been partly funded by a public grant from the French National Research Agency (ANR) under the "France 2030" investment plan, which has the reference EUR MANUTECH SLEIGHT - ANR-17-EURE-0026. The authors would like to acknowledge Tobias Fuerderer and DOCERAM company for providing the CIP samples and the powder for SLA. This work is a follow-up of LONGLIFE(FP7) and SISCERA(H2020) european projects, dedicated to the development of ductile zirconia for orthopedic and dental applications.

References

[1] J. Chevalier, A. Liens, H. Reveron, F. Zhang, P. Reynaud, T. Douillard, L. Preiss, V. Sergo, V. Lughi, M. Swain, N. Courtois, Forty years after the promise of ceramic steel?: Zirconia-based composites with a metal-like mechanical behavior, Journal of the American Ceramic Society 103 (3) (2020) 1482–1513. doi:10.1111/jace.16903.

[2] P. Palmero, M. Fornabaio, L. Montanaro, H. Reveron, C. Esnouf, J. Chevalier, Towards long lasting zirconia-based composites for dental implants: Part I: Innovative synthesis, microstructural characterization and invitro stability, Biomaterials 50 (1) (2015) 38–46. doi:10.1016/j.biomaterials.2015.01.018.

[3] H. Reveron, M. Fornabaio, P. Palmero, T. Fürderer, E. Adolfsson, V. Lughi, A. Bonifacio, V. Sergo, L. Montanaro, J. Chevalier, Towards long lasting zirconia-based composites for dental implants: Transformation induced plasticity and its consequence on ceramic reliability, Acta Biomaterialia 48 (2017) 423–432. doi:10.1016/j.actbio.2016.11.040.

[4] R. H. J. Hannink, P. M. Kelly, B. C. Muddle, Transformation Toughening in Zirconia-Containing Ceramics, J. Am. Ceram. Soc. 83 (3) (2000) 461–487. doi:10.1111/j.1151-2916.2000.tb01221.x.

[5] A. Liens, H. Reveron, T. Douillard, N. Blanchard, V. Lughi, V. Sergo, R. Laquai, B. R. Müller, G. Bruno, S. Schomer, T. Fürderer, E. Adolfsson, N. Courtois, M. Swain, J. Chevalier, Phase transformation induces plasticity with negligible damage in ceria-stabilized zirconia-based ceramics, Acta Materialia 183 (November) (2020) 261–273. doi:10.1016/j.actamat.2019.10.046.

[6] P. F. Becher, M. V. Swain, Grain-Size-Dependent Transformation Behavior in Polycrystalline Tetragonal Zirconia, J. Am. Ceram. Soc 75 (1992) 493–502. doi:10.1111/j.1151-2916.1992.tb07832.x.

[7] K. Tsukuma, M. Shimada, Strength , fracture toughness and Vickers hardness of CeO2-stabilized tetragonal, Journal of Materials Science 20 (1985) (1985) 1178–1184. doi:10.1007/BF01026311.

[8] M. V. Swain, L. R. F. Rose, Strength Limitations of Transformation-Toughened Zirconia Alloys, Journal of the American Ceramic Society 69 (7) (1986) 69–76. doi:10.1111/j.1151-2916.1986.tb04785.x.

[9] Moeschter Group GmbH, https://www.moeschter-group.com/en/materials/evocera/ (8 2022).

[10] I. Touaiher, M. Saâdaoui, J. Chevalier, L. Preiss, H. Reveron, Fracture behavior of Ce-TZP/alumina/aluminate composites with different amounts of transformation toughening. Influence of the testing methods, Journal of the European Ceramic Society 38 (4) (2018) 1778–1789. doi:10.1016/j.jeurceramsoc.2017.09.052.

[11] A. Liens, M. Swain, H. Reveron, J. Cavoret, P. Sainsot, N. Courtois, D. Fabrègue, J. Chevalier, Development of transformation bands in ceria-stabilized-zirconia based composites during bending at room temperature, Journal of the European Ceramic Society 41 (1) (2021) 691–705. doi:10.1016/j.jeurceramsoc.2020.08.062.

[12] M. Y. Mommaerts, Additively manufactured sub-periosteal jaw implants, International Journal of Oral and Maxillofacial Surgery 46 (7) (2017) 938–940. doi:10.1016/j.ijom.2017.02.002.

[13] M. Sharma, M. Soni, Direct metal laser sintering of TI6Al4V alloy for patient-specific temporo mandibular joint prosthesis and implant, Materials Today: Proceedings 38 (2020) 333–339. doi:10.1016/j.matpr.2020.07.417.

[14] M. A. Geven, V. Varjas, L. Kamer, X. Wang, J. Peng, D. Eglin, D. W. Grijpma, Fabrication of patient specific composite orbital floor implants by stereolithography, Polymers for Advanced Technologies 26 (12) (2015) 1433–1438. doi:10.1002/pat.3589.

[15] W. Harrer, M. Schwentenwein, T. Lube, R. Danzer, Fractography of zirconia-specimens made using additive manufacturing (LCM) technology, Journal of the European Ceramic Society 37 (14) (2017) 4331–4338. doi:10.1016/j.jeurceramsoc.2017.03.018.

[16] M. Saâdaoui, F. Khaldoun, J. Adrien, H. Reveron, J. Chevalier, X-ray tomography of additive-manufactured zirconia: Processing defects

– Strength relations, Journal of the European Ceramic Society 40 (8) (2020) 3200–3207. doi:10.1016/j.jeurceramsoc.2019.04.010.

[17] S. Cailliet, M. Roumanie, C. Croutxé-Barghorn, G. Bernard-Granger, R. Laucournet, Y-TZP, Ce-TZP and as-synthesized Ce-TZP/Al2O3 materials in the development of high loading rate digital light processing formulations, Ceramics International 47 (3) (2021) 3892–3900. doi:10.1016/j.ceramint.2020.09.251.

[18] M. Picquart, T. López, R. Gómez, E. Torres, A. Moreno, J. Garcia, Dehydration and crystallization process in Sol-Gel zirconia : Thermal and spectroscopic study, Tech. rep. (2004). doi:10.1023/B:JTAN.0000032260.31955.6e.

[19] M. Khan, M. Ra, S. T. Khan, S. F. Adil, M. Kuniyil, M. Khan, A. A. Al-warthan, M. Ra, M. N. Tahir, Enhanced Antimicrobial Activity of Biofunctionalized Zirconia Nanoparticles (January) (2020). doi:10.1021/acsomega.9b03840.

[20] M. Kunz, H. Kretschmann, W. Assmus, C. Klingshirn, Absorption and emission spectra of Yttria-stabilized zirconia and Magnesium oxide, Tech. rep. (1987). doi:10.1016/0022-2313(87)90185-2.

[21] A. S. Thill, F. O. Lobato, M. O. Vaz, W. P. Fernandes, V. E. Carvalho, E. A. Soares, F. Poletto, S. R. Teixeira, F. Bernardi, Shifting the band gap from UV to visible region in cerium oxide nanoparticles, Applied Surface Science 528 (June) (2020) 146860. doi:10.1016/j.apsusc.2020.146860.

[22] International Organization for Standardization. ISO 6872:2015._ Dentistry-Ceramic materials _. Geneva: ISO; 2015.

[23] I. J. Davies, Confidence limits for Weibull parameters estimated using linear least squares analysis, Journal of the European Ceramic Society 37 (15) (2017) 5057–5064. doi:10.1016/j.jeurceramsoc.2017.05.051.

[24] H. Toraya, M. Yoshimura, S. Somiya, Calibration Curve for Quantitative Analysis of the Monoclinic-Tetragonal ZrO2 System by X-Ray Diffraction, Journal of the American Ceramic Society 67 (6) (1984) C-119–C-121. doi:10.1111/j.1151-2916.1984.tb19715.x.

[25] Internal Report, "Microstructure of starting powder, sintered sample and bending strength", SISCERA Project (EU Grant Agreement No. 737954 09), Tech. rep. (2017).

[26] M. Misevicius, O. Scit, I. Grigoraviciute-Puroniene, G. Degutis, I. Bogdanoviciene, A. Kareiva, Sol-gel synthesis and investigation of un-doped and Ce-doped strontium aluminates, Ceramics International 38 (7) (2012) 5915–5924. doi:10.1016/j.ceramint.2012.04.042.

[27] M. Misevičius, J. E. Jørgensen, A. Kareiva, Sol-gel synthesis, structural and optical properties of cerium-doped strontium aluminates, Sr3Al2O6 and SrAl12O19, Medziagotyra 19 (4) (2013) 438–442. doi:10.5755/j01.ms.19.4.2670.

[28] J. Sun, J. Binner, J. Bai, 3d printing of zirconia via digital light processing: optimization of slurry and debinding process, Journal of the European Ceramic Society 40 (15) (2020) 5837–5844. doi:https://doi.org/10.1016/j.jeurceramsoc.2020.05.079.

[29] H. Wu, Y. Cheng, W. Liu, R. He, M. Zhou, S. Wu, X. Song, Y. Chen, Effect of the particle size and the debinding process on the density of alumina ceramics fabricated by 3d printing based on stereolithography, Ceramics International 42 (15) (2016) 17290–17294. doi:https://doi.org/10.1016/j.ceramint.2016.08.024.

[30] R. Rice, Microstructure dependence of mechanical behavior of ceramics, in: N. Y. ed. R. McCrone. Academic Press (Ed.), Treatise on Materials Science and Technology, 1977, pp. 199–381. doi:10.1016/b978-0-12-341811-1.50010-8.

[31] W. Weibull, A Statistical Distribution Function of Wide Applicability, Journal of Applied Mechanics 18 (1951) 293–297. doi:10.1115/1.4010337.

[32] F. Zhang, H. Reveron, B. C. Spies, B. Van Meerbeek, J. Chevalier, Trade-off between fracture resistance and translucency of zirconia and lithium-disilicate glass ceramics for monolithic restorations, Acta Biomaterialia 91 (2019) 24–34. doi:10.1016/j.actbio.2019.04.043.

[33] R. C. Petersen, Accurate critical stress intensity factor griffith crack theory measurements by numerical techniques, Sampe J (2013) 737–752.

[34] A. A. Griffith, G. I. Taylor, Vi. the phenomena of rupture and flow in solids, Philosophical Transactions of the Royal Society of London. Series A, Containing Papers of a Mathematical or Physical Character 221 (582-593) (1921) 163–198. doi:10.1098/rsta.1921.0006.

Declaration of interests

☒ The authors declare that they have no known competing financial interests or personal relationships that could have appeared to influence the work reported in this paper.

☐The authors declare the following financial interests/personal relationships which may be considered as potential competing interests: